

TPCNet: Triple physical constraints for Low-light Image Enhancement

Jing-Yi Shi^{1,2} Ming-Fei Li^{1,2*} Ling-An Wu^{1,2}

¹Institute of Physics, China Academy of Sciences, Beijing 100190, China

²School of Physical Sciences, University of Chinese Academy of Sciences, Beijing 100049, China

Abstract

Low-light image enhancement is an essential computer vision task to improve image contrast and to decrease the effects of color bias and noise. Many existing interpretable deep-learning algorithms exploit the Retinex theory as the basis of model design. However, previous Retinex-based algorithms, that consider reflected objects as ideal Lambertian ignore specular reflection in the modeling process and construct the physical constraints in image space, limiting generalization of the model. To address this issue, we preserve the specular reflection coefficient and reformulate the original physical constraints in the imaging process based on the Kubelka-Munk theory, thereby constructing constraint relationship between illumination, reflection, and detection, the so-called triple physical constraints (TPCs) theory. Based on this theory, the physical constraints are constructed in the feature space of the model to obtain the TPC network (TPCNet). Comprehensive quantitative and qualitative benchmark and ablation experiments confirm that these constraints effectively improve the performance metrics and visual quality without introducing new parameters, and demonstrate that our TPCNet outperforms other state-of-the-art methods on 10 datasets. Code is available at <https://github.com/2020shijingyi/TPCNet>

1. Introduction

A major challenge for computer vision is how to overcome the low signal-to-noise ratio and inaccurate colors of images caused by underexposure [30, 44]. For this reason, low-light image enhancement (LLIE), which aims to improve image contrast while minimizing the effects of color bias, is an essential task [11]. During the past decades, conventional non-learning methods, like gamma correction [36] and histogram equalization [1, 16], have been widely applied for low-light enhancement, performing transformation on pixel values or adjusting their distribution to realize

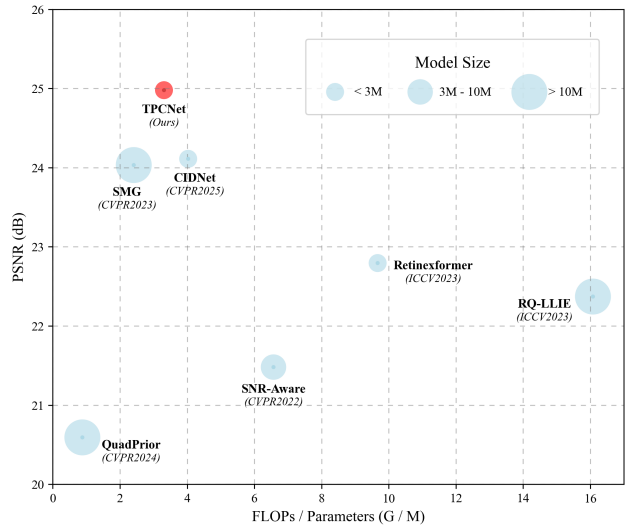


Figure 1. Our TPCNet shows its efficient design and outstanding performance compared to recent SOTA methods, including CIDNet (HVI [53], CVPR2025), QuadPrior (Quadruple Priors [45], CVPR2024), SMG (SMG-LLIE [52], CVPR2023), Retinexformer [3] (ICCV2023), RQ-LLIE [26] (ICCV2023), and SNR-Aware (SNR-Net [51], CVPR2022) for Low-light Image enhancement on LOLv2-real [55] benchmarks.

dynamic range expansion and contrast adjustments. In addition, various Retinex-based methods [11, 13] decompose low-light images into illuminated and reflected components and enhance the reflected component or optimize the illuminated features to realize enhancement. The above methods all exhibit interpretable physical processes, but these artificially designed constraints or priors may cause color bias and noise as their adaptability is insufficient for LLIE when dealing with complex illumination.

With the development of deep learning, convolutional neural networks (CNNs) and vision transformers (ViTs), have been applied in various tasks and have made significant advancements [23, 35, 40, 46, 57]. For LLIE, deep learning combined with an interpretable physical model has gradually evolved as an effective approach, rather than viewing the learnable modules as a simple black-box. Recently, COMO-ViT [47] constructed an illumination-aware

*Corresponding author. Email: lmf.li@iphy.ac.cn

gamma correction module whose gamma factor is calculated by the learnable modules to avoid the bias caused by manual design. Meanwhile, the deep learning framework inspired by the Retinex theory utilizes different CNNs (or ViTs) as the independent estimators for illumination $\hat{\mathbf{L}}$ and reflectivity $\hat{\mathbf{R}}$ and computes the enhanced images by $\hat{\mathbf{L}} \odot \hat{\mathbf{R}}$ (\odot denotes the element-wise multiplication). Under the guidance of this theory, various methods [3, 50, 56, 60] have been proposed; however, Retinex-based learnable methods typically regard the image as the invariant and decompose it into reflectivity and illumination components. To construct the explicit physical constraint ($\mathbf{I} = \hat{\mathbf{L}} \odot \hat{\mathbf{R}}$) between reflectivity and illumination, which is based on actual space ($\mathbf{R} \in \mathcal{R}^{3 \times H \times W}$ and $\mathbf{L} \in \mathcal{R}^{1 \times H \times W}$) and relies on input \mathbf{I} , it is necessary to supervise reflectivity (or illumination) features during training with a complex loss function [7, 35].

Inspired by physical quadruple priors [21, 45], which extract illumination invariant features from input, we exploit the intrinsic features in the imaging process to construct implicit constraints, without complex loss functions for supervising the process variables during training, and so can decrease the difficulty in designing the loss functions. Specifically, we reformulate the physical constraints in the imaging process based on the Kubelka-Munk (KM) theory [9, 10] and construct the triple physical constraint (TPC) among the detection $\hat{\mathbf{E}}$ (of the reflected light), illumination $\hat{\mathbf{e}}$ (by the light source), and reflectivity $\hat{\mathbf{R}}$ (of the material). Different from the previous Retinex theory, which only considers ideal Lambertian reflection, we retain the specular reflection coefficient and replace it with learnable variables, thus allowing the $\hat{\mathbf{e}}$ to characterize two complementary illumination components $\hat{\mathbf{L}}$ and $\hat{\mathbf{L}}$. Guided by this TPC theory, we design the reflectivity feature estimators (RFE) and light feature estimators (LFE) to estimate the initial $\hat{\mathbf{R}}$ and $\hat{\mathbf{L}}$, respectively, while the initial estimates are enhanced by utilizing the backbone structure, a Dual-Stream Cross-Guided Transformer (DCGT) whose core component is a Cross-Guided Multi-Head Self-Attention (CG-MSA). Based on the relationship between $\hat{\mathbf{E}}$, $\hat{\mathbf{e}}$, and $\hat{\mathbf{R}}$, we construct constraints in an implicit feature space ($\mathcal{R}^{C \times H \times W}$) rather than in the image space, which can be easily extended to different datasets and improves model robustness. Finally, we derive our method, TPCNet, by combining the core components RFE, LFE, and DCGT with the Color-Association Mechanism (CAM), which is exploited to decrease color bias. As shown in Fig. 1, our TPCNet outperforms recent state-of-the-art (SOTA) lightweight approaches on the real-image dataset LOL-v2-real [55].

Our contributions can be summarized as follows:

- We reformulate the origin of physical constraints in the imaging process, based on the KM theory, and construct the TPC among the detection, illumination, and reflectivity. This offers an effective and interpretable direc-

tion to design robust networks.

- We further propose the TPCNet, a novel LLIE CNN-Transformer framework, which establishes the physical constraints in an implicit feature space to improve its robustness and generalization. Although the TPCNet possesses not so many parameters (2.62M), it exhibits computationally-efficient capacity (only 8.68GFLOPs), benefiting from the efficient design of CG-MSA, which consumes only 25% of the computation of conventional multi-head self-attention (MSA) with the same input size.
- Quantitative and qualitative experiments results demonstrate that our TPCNet outperforms other SOTA approaches on different metrics across 10 datasets.

2. Related Work

2.1. Low-Light Image Enhancement via Physical Modelling

Retinex-based model. The Retinex theory [19], a human visual simulation model widely applied in LLIE, is an effective enhancement algorithm. It regards the observed image as one that can be decomposed into illuminated and reflected components: $\mathbf{I} = \hat{\mathbf{L}} \odot \hat{\mathbf{R}}$, where $\hat{\mathbf{L}}$ and $\hat{\mathbf{R}}$ refer to the illumination and the reflectance, respectively. Early approaches based on Retinex viewed the reflectance as the final enhanced result, usually causing the result to look unnatural and to be excessively enhanced, *e.g.*, single-scale Retinex [13]. Later, Guo *et al.* proposed the LIME algorithm [11], which enhances the image via illumination map estimation, improving the visual aesthetics and imaging efficiency [13, 33]. Recently, deep learning combined with interpretable physical modeling has been increasingly seen as an effective direction for LLIE. RetinexNet [50], which combines the Retinex model with data-driven schemes, realizes more accurate reconstruction and more efficient image decomposition than conventional Retinex algorithms by utilizing elaborately hand-crafted loss functions. The above Retinex Imaging model assumes images are corruption-free for decomposing. Corruption-free images cannot be achieved in the inadequate lighting scenes and flaws in the imaging system. To decompose the images the Retinex model assumes that they are corruption-free, but such images cannot be achieved when the lighting is inadequate and there are flaws in the imaging system. To overcome this limitation, Li *et al.* [24] proposed a robust Retinex model and pointed out that for real environments the model should include a noise term \mathbf{N} as follows: $\mathbf{I} = \hat{\mathbf{L}} \odot \hat{\mathbf{R}} + \mathbf{N}$. Then, Cai *et al.* [3] formulated a simple yet one-stage Retinex-based framework $\mathbf{I} = (\hat{\mathbf{L}} + \delta_{\hat{\mathbf{L}}}) \odot (\hat{\mathbf{R}} + \delta_{\hat{\mathbf{R}}})$ which introduced perturbation terms $\delta_{\hat{\mathbf{L}}}$ and $\delta_{\hat{\mathbf{R}}}$ for illumination and reflectance, respectively. However, these frameworks construct physical constraints in real space and rely on input features, so the constraints formed by learning generalize poorly to other

datasets.

Kubelka–Munk-based model. The KM theory [9], which assumes that light within a material is isotropically scattered and characterizes the material layers by a wavelength-dependent scatter coefficient and absorption coefficient, is used for materials that both reflect and transmit light. As a general image formation model, it is adopted for studying the reflectance of light in real-world scenes, based on which Geusebroek *et al.* proposed a photometric reflectance model to formulate color invariance [10]. Recently, Wang *et al.* [45] devised illumination invariance, a physical quadruple prior, which originated from the KM theory, and can realize robust zero-reference LLIE. However, the KM model is mainly applied to calculate the invariances of the imaging process, while Retinex is a special case of this theory. The potential of the KM theory for LLIE to realize image decomposition or construct physical constraints has not yet been fully explored.

3. Method

Figure 2 displays the specific architecture of our method. As illustrated in Fig. 2(a), our TPCNet is composed of the LFE, RFE, DCGT, and CAM modules, where DCGT is designed as the core component of the enhancer, comprising the basis units, namely Cross-Guided Attention Blocks (CGABs). The latter, which include variants in skip connections, positional encoding, and feature crossover, such as, CGAB (V), CGAB (V-M), and CGAB (M), are composed of a normalization layer, a CG-MSA module, and an IEL module [53] similar to the Gated Forward Network. The CGAB(V) represents the variant that is different in positional encoding and skip connections, and CGAB (M) stands for the CG-MSA module with the pair-downsample removed.

3.1. Triple Physical Constraint Framework

To introduce our TPC concept, we start from the image formation model based on the Kubelka-Munk theory [9]

$$E(\lambda, \mathbf{x}) = e(\lambda, \mathbf{x})((1 - \rho_f(\mathbf{x}))^2 R_\infty(\lambda, \mathbf{x}) + \rho_f(\mathbf{x})), \quad (1)$$

where $E(\lambda, \mathbf{x})$ stands for the spectrum of light reflected from an object in the viewing direction, λ and \mathbf{x} refer to the wavelength of the light and spatial location on the image plane, respectively, $e(\lambda, \mathbf{x})$ denotes the spectrum of the light source, $R_\infty(\lambda, \mathbf{x})$ is the material reflectivity, and $\rho_f(\mathbf{x})$ represents the specular reflection coefficient. Following the Retinex-based image formation approximation [50], we ignore the effect of the wavelength to simplify Eq. (1). But for $\rho_f(\mathbf{x})$, the Retinex theory [19, 45] assumes the objects to be Lambertian and that $\rho_f(\mathbf{x}) \approx 0$, whereas we view $\rho_f(\mathbf{x})$ as a small quantity that cannot be ignored.

Then, by expanding $(1 - \rho_f(\mathbf{x}))^2$ as a Taylor series and omitting higher-order term, we reformulate Eq. (1) as

$$E(\mathbf{x}) = (1 - 2\rho_f(\mathbf{x}))e(\mathbf{x})R_\infty(\mathbf{x}) + \rho_f(\mathbf{x})e(\mathbf{x}). \quad (2)$$

Subsequently, by setting $1 - 2\rho_f(\mathbf{x}) = \alpha(\mathbf{x})$, Eq. (2) can be written as

$$E(\mathbf{x}) = \underbrace{\alpha(\mathbf{x})e(\mathbf{x})}_{L(\mathbf{x})} R_\infty(\mathbf{x}) + \underbrace{(1 - \alpha(\mathbf{x}))e(\mathbf{x})}_{\bar{L}(\mathbf{x})} / 2, \quad (3)$$

where $L(\mathbf{x}) = \alpha(\mathbf{x})e(\mathbf{x})$ can be regarded as an illumination map, while $\bar{L}(\mathbf{x}) = (1 - \alpha(\mathbf{x}))e(\mathbf{x})$ is its complementary illumination map, and both satisfy the constraint

$$L(\mathbf{x}) + \bar{L}(\mathbf{x}) = e(\mathbf{x}), \quad (4)$$

By transforming Eq. (3), we obtain another constraint as

$$R_\infty(\mathbf{x}) = \frac{E(\mathbf{x}) - \bar{L}(\mathbf{x})/2}{L(\mathbf{x})}, \quad (5)$$

Equations (3) to (5) constitute a TPC for detection of the reflected light, the illumination from the light source, and the material reflectivity characteristic, respectively. This TPC thus provides a heuristic guidance for network design.

3.2. Overview of the Triple Physical Constraint Network

To endow the network with TPC (TPCNet), the computational graph can be formulated as:

$$\begin{aligned} \psi(\mathbf{I}) \rightarrow (\hat{\mathbf{e}}, \hat{\alpha}) \xrightarrow{\text{Eq. (4)}} (\hat{\mathbf{L}}, \hat{\bar{L}}) \rightarrow \zeta(\hat{\mathbf{L}}, \hat{\bar{L}}) \rightarrow \hat{\mathbf{R}} \\ \hat{\mathbf{R}} \rightarrow \mathcal{E}(\hat{\mathbf{R}}, \hat{\bar{L}}) \rightarrow (\hat{\mathbf{R}}^*, \hat{\mathbf{e}}^*) \xrightarrow[\text{add } \hat{\alpha}]{\text{Eq. (3)}} \hat{\mathbf{E}} \end{aligned} \quad (6)$$

where ψ refers to the LFE, ζ denotes the RFE and \mathcal{E} stands for the enhancer. Taking low-light images $\mathbf{I} \in \mathcal{R}^{3 \times H \times W}$ as input, ψ estimates the initial light features $\hat{\mathbf{e}} \in \mathcal{R}^{C \times H \times W}$ and corresponding weight $\hat{\alpha} \in \mathcal{R}^{1 \times H \times W}$ with value [0-1]. Subsequently, substituting the $\hat{\mathbf{e}}$ and $\hat{\alpha}$ into Eq. (4) as the first constraint, we can calculate the complementary illumination map $\hat{\bar{L}} \in \mathcal{R}^{C \times H \times W}$. Then \mathbf{I} and $\hat{\bar{L}}$ are fed into ζ with the Eq. (5) constraint to produce the reflectivity feature $\hat{\mathbf{R}} \in \mathcal{R}^{C \times H \times W}$. Ultimately, the enhanced $\hat{\mathbf{R}}^* \in \mathcal{R}^{C \times H \times W}$ and $\hat{\mathbf{e}}^* \in \mathcal{R}^{C \times H \times W}$ are calculated by a four-scale U-shaped architecture \mathcal{E} and we substitute $\hat{\mathbf{R}}^*$, $\hat{\mathbf{e}}^*$ and $\hat{\alpha}$ into Eq. (3) to obtain the reflected-light feature $\hat{\mathbf{E}}^* \in \mathcal{R}^{C \times H \times W}$, thus realizing the third physical constraint on the network.

However, since the effect of wavelength has been ignored in our model, directly mapping $\hat{\mathbf{E}}^*$ to $\mathbf{I}_{en} \in \mathcal{R}^{3 \times H \times W}$ may result in color deviation or overexposure. To overcome this limitation, we introduce a multi-scale color-association mechanism. First, we convert the RGB color

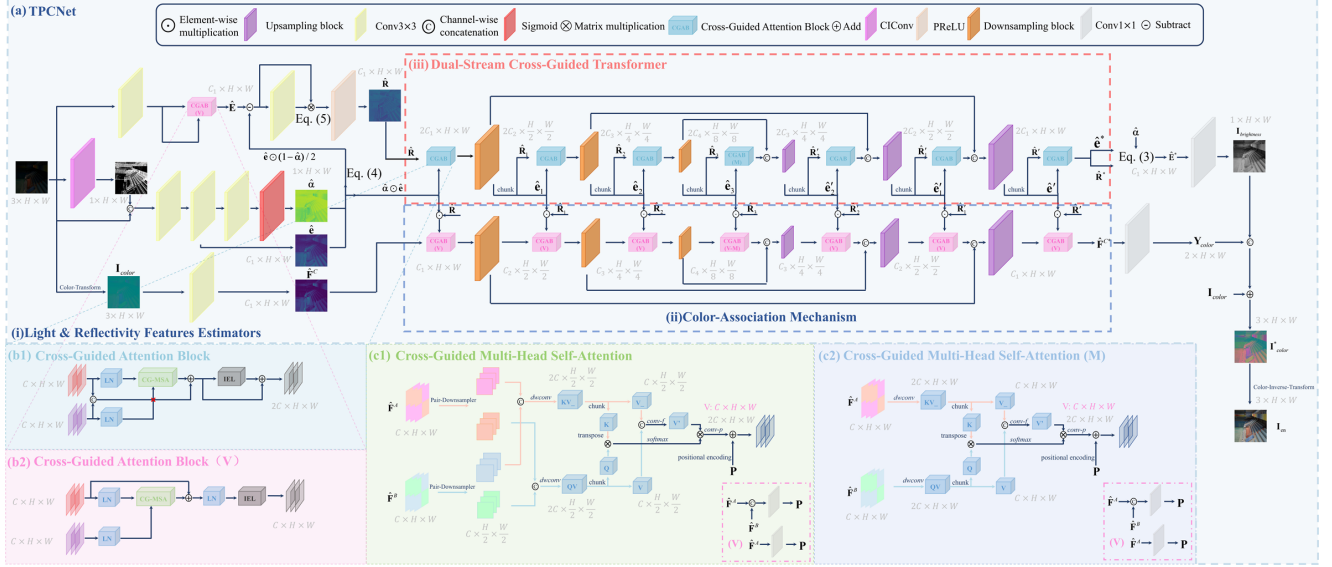


Figure 2. (a) Overview of our proposed TPCNet, which contains a Light & Reflectivity Features Estimator (i), the Color-Association Mechanism (CAM) (ii), and the Dual-Stream Cross-Guided Transformer (iii). (b1) The Cross-Guided Attention Blocks (CGABs) are comprised of a normalization layer (LN), a Cross-Guided Multi-Head Self-Attention (CG-MSA) module, and an IEL module [53]. (b2) CGAB (V) with variation in skip connection. (c1)-(c2) Detailed structure of the CG-MSA and its variation.

space of \mathbf{I} into another color space $\mathbf{I}_{color} \in \mathcal{R}^{3 \times H \times W}$ (e.g., YCbCr [15], HSV [37], HVI [53], etc.) to realize the separation of brightness and color information. Subsequently, the color features $\hat{\mathbf{F}}^C \in \mathcal{R}^{C \times H \times W}$ are extracted from \mathbf{I}_{color} , and are then fed into the DCGTs to obtain the enhanced color feature $\hat{\mathbf{F}}^{C*} \in \mathcal{R}^{C \times H \times W}$ with the multi-scale $\hat{\mathbf{R}}^* \odot \hat{\mathbf{e}}^*$ information as feature guidance. Next, the $\hat{\mathbf{F}}^{C*}$ and $\hat{\mathbf{E}}^*$ are mapped to the color information $\mathbf{Y}_{color} \in \mathcal{R}^{2 \times H \times W}$ and brightness $\mathbf{I}_{brightness} \in \mathcal{R}^{1 \times H \times W}$, respectively, and we concatenate \mathbf{Y}_{color} and $\mathbf{I}_{brightness}$ for each pixel along the channel dimension to acquire the $\mathbf{I}^*_{color} \in \mathcal{R}^{3 \times H \times W}$ and introduce the residual connection $\mathbf{I}^*_{color} = \mathbf{I}^*_{color} + \mathbf{I}_{color}$. Finally, the \mathbf{I}^*_{color} is transformed back into the \mathbf{I}_{en} .

The architecture of ψ is shown in Fig. (2), where ψ first extracts the invariance properties W of the illumination intensity from \mathbf{I} by a CConv [21], and a $conv3 \times 3$ (convolution with kernel size = 3) is used to fuse the concatenation of \mathbf{I} and W . Since the fused feature possesses rich semantic contextual information, we utilize a $conv3 \times 3$ operation to generate $\hat{\mathbf{e}}$, and the corresponding weight $\hat{\alpha}$ is calculated by another $conv3 \times 3$ followed by Sigmoid activation.

The composition of ζ is exhibited in Fig. 2(a). First, ζ employs a $conv3 \times 3$ followed by the CGAB to estimate $\hat{\mathbf{E}}$ from \mathbf{I} and calculates $\hat{\mathbf{E}} - \frac{\hat{\mathbf{L}}}{2}$. Subsequently, $\hat{\mathbf{E}} - \frac{\hat{\mathbf{L}}}{2}$ is fed into another $conv3 \times 3$ to produce $\hat{\mathbf{L}}'$ where $\hat{\mathbf{L}}' \odot \hat{\mathbf{L}} = 1$. To enhance the physical constraints, we substitute $\hat{\mathbf{E}} - \frac{\hat{\mathbf{L}}}{2}$ and $\hat{\mathbf{L}}'$ into Eq. (5) to compute $\hat{\mathbf{R}}$.

Discussion. (i) Compared with the previous deep learning

methods based on the Retinex theory [7, 11, 50, 56, 60] that view the $\hat{\mathbf{R}}$ and $\hat{\mathbf{L}}$ as independent estimations and employ deep convolutional neural networks to estimate separately or to estimate $\hat{\mathbf{L}}$ only, the TPC framework regards the $\hat{\mathbf{R}}$ and $\hat{\mathbf{L}}$ as the estimations with mathematical connection, and then the $\hat{\mathbf{R}}$ can be calculated by $(\hat{\mathbf{E}} - \frac{\hat{\mathbf{L}}}{2}) \odot \hat{\mathbf{L}}'$. This framework utilizes the inherent relationships between $\hat{\mathbf{R}}$ and $\hat{\mathbf{L}}$ for self-constraint without requiring complicated loss functions, which can be effective in decreasing training difficulty. Moreover, the calculation process $\hat{\mathbf{R}} = (\hat{\mathbf{E}} - \frac{\hat{\mathbf{L}}}{2}) \odot \hat{\mathbf{L}}'$ possesses some advantages. From one perspective, $(\hat{\mathbf{E}} - \frac{\hat{\mathbf{L}}}{2})$ can decrease the estimation bias to a certain extent by computing the difference between $\hat{\mathbf{E}}$ and $\frac{\hat{\mathbf{L}}}{2}$. From another perspective, $\hat{\mathbf{R}} = (\hat{\mathbf{E}} - \frac{\hat{\mathbf{L}}}{2}) \odot \hat{\mathbf{L}}'$ avoids directly dividing $(\hat{\mathbf{E}} - \frac{\hat{\mathbf{L}}}{2})$ by $\hat{\mathbf{L}}$, which can enlarge the deviation [3] and can produce a more robust $\hat{\mathbf{R}}$.

(ii) Inspired by the Retinex theory [19], we employ $\hat{\mathbf{R}} \odot \hat{\mathbf{e}}$, a rough light-up feature, as an initial guidance to produce the corresponding color features in our CAM. However, multiplying two estimated values directly might intensify the deviation due to the existence of estimation bias, and the expanded deviation will further contaminate the subsequent output by forward propagation, affecting model performance. To address these limitations, we adopt multi-scale light-up features and recalculate each scale-guided feature by employing enhanced light-up instead of the skip connections from the initial $\hat{\mathbf{R}} \odot \hat{\mathbf{e}}$ to the next scale, thus diminishing the deviation accumulation.

3.3. Dual-Stream Cross-Guided Transformer

Recently, due to their superiority in capturing long-range dependencies, transformers have been increasingly exploited in image enhancement or restoration. Their computing mechanism can be flexibly used to calculate the correlation between features and to realize cross guidance. Some transformer-based guided mechanism, like Retinexformer [3], realize feature guidance by value elements \mathbf{V} multiplied with \mathbf{F}_{lu} ; others, like CIDNet [53], calculate \mathbf{KV} elements and \mathbf{Q} from two different features using separate learnable layers, and then realize cross guidance based on a self-attention mechanism (SAM). These guidance mechanisms have inherent limitations. Facing different features, the separate learnable layers with distinct learning abilities can cause attention bias, and the output can be affected by the portion that possesses stronger learning capabilities. To address this limitation, we design a DCGT as the enhancer \mathcal{E} .

Network Structure. As illustrated in Fig. 2(a), DCGT exploits a four-scale U-Structure. Initial $\hat{\mathbf{L}}$, $\hat{\mathbf{R}}$ and $\hat{\mathbf{F}}^C$, are input into DCGT. During downsampling, $\hat{\mathbf{L}}$ and $\hat{\mathbf{R}}$ are processed by a CGAB and a downsampling block which consists of $conv3 \times 3$ (for channel conversion), bilinear interpolation, and PReLU activation, to generate $\hat{\mathbf{F}}_i^{RL} \in \mathcal{R}^{2C_i \times \frac{H}{2^i} \times \frac{W}{2^i}}$ where $i = 1, 2, 3$. Then $\hat{\mathbf{F}}_i^{RL}$ is partitioned into $\hat{\mathbf{R}}_i$ and $\hat{\mathbf{e}}_i$ along the channel dimension; $\hat{\mathbf{R}}_i$ and $\hat{\mathbf{e}}_i$ as the new inputs are fed into the CGAB. For the downsampling color-association portion, $\hat{\mathbf{F}}^C$ and $\hat{\mathbf{R}} \odot \hat{\mathbf{L}}$ undergo a CGAB and the downsampling block to produce the $\hat{\mathbf{F}}_i^C \in \mathcal{R}^{C_i \times \frac{H}{2^i} \times \frac{W}{2^i}}$. As the guidance for $\hat{\mathbf{F}}_i^C$, $\hat{\mathbf{R}}_i \odot \hat{\mathbf{e}}_i$ is applied in the next CGAB. Then $\hat{\mathbf{R}}_3$ and $\hat{\mathbf{e}}_3$ pass through CGAB (M) while $\hat{\mathbf{F}}_3^C$ and $\hat{\mathbf{R}}_3 \odot \hat{\mathbf{e}}_3$ are fed into CGAB (V-M), respectively. Subsequently, a symmetrical structure is designed for upsampling. The upsampling block is utilized to fuse skip connections and to upscale the features, which is composed of $conv3 \times 3$ (for channel conversion), $conv1 \times 1$ (for connection fusion) bilinear interpolation, and PReLU activation. The color space of TPCNet is Ycbr, and the results of ablation experiments shown in Table 3 verify the effect of different color spaces.

CG-MSA. As displayed in Fig. 2(c1-c2), $\hat{\mathbf{F}}^A \in \mathcal{R}^{C \times H \times W}$ and $\hat{\mathbf{F}}^B \in \mathcal{R}^{C \times H \times W}$ are fed into the CG-MSA which is a core component for all variants of CGAB. To calculate the cross-correlation features between $\hat{\mathbf{F}}^A$ and $\hat{\mathbf{F}}^B$, we first utilize the pair downsampler [31] to divide $\hat{\mathbf{F}}$ into non-overlapping 2×2 patches, and obtain $\hat{\mathbf{F}}_i^j \in \mathcal{R}^{C \times \frac{H}{2} \times \frac{W}{2}}$, where $i=1,2$; $j=A, B$. Subsequently, we concatenate $\hat{\mathbf{F}}_1^A, \hat{\mathbf{F}}_2^B$ and $\hat{\mathbf{F}}_2^A, \hat{\mathbf{F}}_1^B$ along the channel dimension to generate combined features $\hat{\mathbf{F}}_i^M \in \mathcal{R}^{2C \times \frac{H}{2} \times \frac{W}{2}}$ where $i=1, 2$. Then, utilizing the SAM, the combined features are further fused to produce the cross-guided attention map. In our de-

signed MSA, the query (\mathbf{Q}), key (\mathbf{K}) and value (\mathbf{V}) projections are calculated by a projective $conv1 \times 1$ followed by a 3×3 depth-wise convolution ($dwcov3 \times 3$). The $conv1 \times 1$ is used to polymerize pixel-wise cross-channel information and then we utilize $dwcov3 \times 3$ to enhance the polymerized information. To avoid attention bias caused by different learning capability, the formulas for calculating the projections are as follows:

$$\mathbf{QV}^* = W_d^{KV*} W_p^{KV*} \hat{\mathbf{F}}_1^M, KV = W_d^{KV} W_p^{KV} \hat{\mathbf{F}}_2^M, \quad (7)$$

where $W_p^{(\cdot)}$ and $W_d^{(\cdot)}$ represent the learnable parameters of the $conv1 \times 1$ and $dwcov3 \times 3$, respectively. Subsequently, splitting \mathbf{QV}^* and \mathbf{KV} into $\mathbf{Q}, \mathbf{K}, \mathbf{V}, \mathbf{V}^* \in \mathcal{R}^{C \times \frac{H}{2} \times \frac{W}{2}}$, we combine the \mathbf{V}^* and \mathbf{V} to produce \mathbf{V}' by using a $conv3 \times 3$ and divide the number of channels into each "head". Then, the cross-guided attention map for each head can be formulated as

$$\text{Attention}(\mathbf{Q}_j, \mathbf{K}_j, \mathbf{V}'_j) = \mathbf{V}'_j \odot \text{Softmax}\left(\frac{\mathbf{Q}_j \mathbf{K}_j^T}{\alpha_H}\right), \quad (8)$$

where $\mathbf{Q}_j, \mathbf{K}_j, \mathbf{V}'_j \in \mathcal{R}^{h_k \times \frac{HW}{4}}$, $h_k = \frac{C}{k}$, $j = 1, 2, \dots, k$; k is the head number and α_H is a learnable scaling parameter that adaptively scales the magnitude of the dot product of \mathbf{Q}_j and \mathbf{K}_j^T [6, 27]. The k -head features are concatenated along the channel dimension and reshaped to $\hat{\mathbf{F}}_{out}^M \in \mathcal{R}^{2C \times \frac{H}{2} \times \frac{W}{2}}$; $\hat{\mathbf{F}}_{out}^M$ undergoes the pixel-shuffle $conv1 \times 1$ to upscale its resolution, and finally adds a positional encoding calculated by a $conv1 \times 1$ that concatenates $\hat{\mathbf{F}}^A$ and $\hat{\mathbf{F}}^B$ as input, to generate the cross-guided features $\hat{\mathbf{F}}_{out}^{AB} \in \mathcal{R}^{2C \times H \times W}$.

To simplify the analysis of computational complexity, we focus on computation of our SAM in Eq. (8), which involves two matrix multiplications $\mathcal{R}^{h_k \times \frac{HW}{4}} \times \mathcal{R}^{\frac{HW}{4} \times h_k}$ and $\mathcal{R}^{\frac{HW}{4} \times h_k} \times \mathcal{R}^{h_k \times h_k}$. The formulas of the CG-MSA computational complexity are thus as follows,

$$\begin{aligned} \mathcal{O}(\text{CG-MSA}) &= k \cdot \left(\frac{HW}{4} \cdot h_k \cdot h_k\right) + k \cdot (h_k \cdot h_k \cdot \frac{HW}{4}) \\ &= k \frac{HW}{2} h_k^2 = k \frac{HW}{2} \left(\frac{C}{k}\right)^2 = \frac{HWC^2}{2k} \end{aligned} \quad (9)$$

Compared with the previous CNN-Transformer methods [3, 51], the computational complexity of CG-MSA is linear in the spatial size, and only 25% of the conventional MSA computation is required for the same input size. Therefore, CG-MSA can be effective in improving our TPCNet's inference speed, and can serve as a plug-and-play lightweight design module.

Table 1. Quantitative comparison with LOL v2 [55] and VILNC-indoor [35] datasets using different evaluation methods (PSNR \uparrow , SSIM \uparrow , and LPIPS \downarrow). The best and second-best performances are highlighted in red and cyan, respectively. The FLOPs is calculated on a single 256 \times 256 image.

| Methods | Complexity | | LOL-v2-Real | | | LOL-v2-Synthetic | | | VILNC-Indoor | | |
|---------------------|------------|---------|-----------------|-----------------|--------------------|------------------|-----------------|--------------------|-----------------|-----------------|--------------------|
| | Params/M | FLOPs/G | PSNR \uparrow | SSIM \uparrow | LPIPS \downarrow | PSNR \uparrow | SSIM \uparrow | LPIPS \downarrow | PSNR \uparrow | SSIM \uparrow | LPIPS \downarrow |
| KinD [59] | 8.02 | 34.99 | 17.544 | 0.669 | 0.375 | 18.320 | 0.796 | 0.252 | 9.453 | 0.583 | 0.411 |
| RUAS [25] | 0.003 | 0.83 | 15.506 | 0.491 | 0.314 | 13.880 | 0.676 | 0.291 | 8.836 | 0.570 | 0.735 |
| RetinexNet [50] | 0.84 | 584.47 | 16.097 | 0.401 | 0.543 | 17.137 | 0.762 | 0.255 | 16.573 | 0.456 | 0.547 |
| ZeroDCE++ [22] | 0.01 | 0.61 | 12.338 | 0.443 | 0.488 | 15.871 | 0.804 | 0.217 | 15.992 | 0.434 | 0.579 |
| SNR-Net [51] | 4.01 | 26.35 | 21.480 | 0.849 | 0.163 | 24.140 | 0.928 | 0.056 | 23.367 | 0.765 | 0.202 |
| LLFormer [43] | 24.55 | 22.52 | 20.056 | 0.792 | 0.211 | 24.038 | 0.909 | 0.066 | 23.593 | 0.769 | 0.313 |
| Retinexformer [3] | 1.61 | 15.57 | 22.794 | 0.840 | 0.171 | 25.670 | 0.930 | 0.059 | 23.735 | 0.782 | 0.295 |
| PairLIE [8] | 0.33 | 20.81 | 19.885 | 0.778 | 0.317 | 19.074 | 0.794 | 0.230 | 9.255 | 0.570 | 0.681 |
| EnlightenGAN [12] | 114.35 | 61.01 | 18.230 | 0.617 | 0.309 | 16.570 | 0.734 | 0.220 | 18.976 | 0.615 | 0.354 |
| HVI-CIDNet [53] | 1.88 | 7.57 | 24.111 | 0.868 | 0.116 | 25.705 | 0.942 | 0.045 | 23.656 | 0.785 | 0.303 |
| QuadPrior [45] | 1252.75 | 1103.2 | 20.592 | 0.811 | 0.202 | 16.108 | 0.758 | 0.114 | 11.293 | 0.552 | 0.487 |
| LANet [54] | 0.58 | 43.23 | 18.074 | 0.735 | 0.364 | 18.088 | 0.807 | 0.183 | 18.410 | 0.734 | 0.484 |
| ZERO-IG [35] | 0.087 | 11.37 | 16.943 | 0.738 | 0.395 | 17.610 | 0.743 | 0.410 | 12.002 | 0.595 | 0.504 |
| SMG [52] | 17.8 | 42.93 | 24.032 | 0.818 | 0.169 | 24.979 | 0.891 | 0.092 | 23.440 | 0.688 | 0.212 |
| RQ-LLIE [26] | 13.48 | 216.78 | 22.371 | 0.854 | 0.142 | 25.937 | 0.941 | 0.044 | 23.540 | 0.791 | 0.288 |
| TPCNet(Ours) | 2.62 | 8.76 | 24.978 | 0.882 | 0.102 | 26.032 | 0.943 | 0.041 | 24.634 | 0.785 | 0.194 |

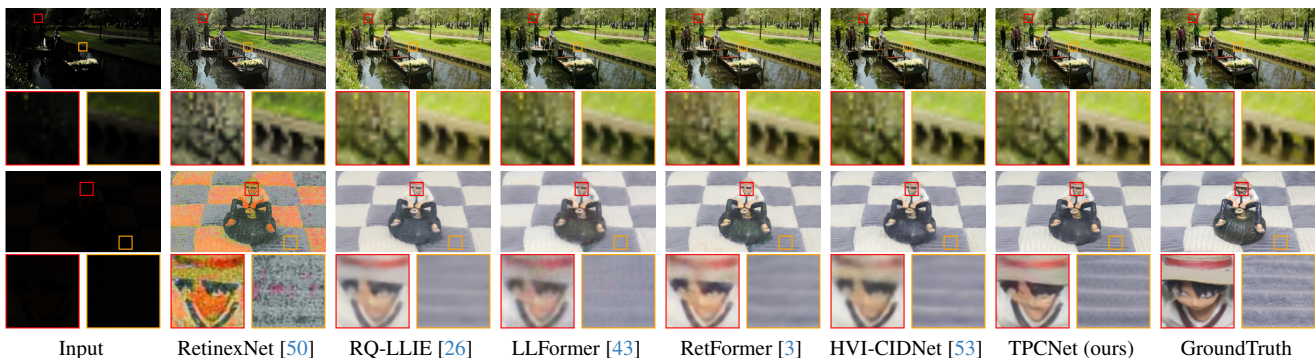


Figure 3. Comparison of the enhanced images with various SOTA methods on LOL-v2-Synthetic (top row) and VILNC-Indoor (bottom row).

4. Experiment

4.1. Datasets and Settings Details

We evaluated our method on commonly-used LLIE benchmark datasets including LOL v2 [55], DICM [20], LIME [11], MEF [29], NPE [42], and VV [39]. We also conducted further experiments on a real-world LLIE dataset VILNC [35], an extreme dataset SID (Sony-Total-Dark) [5], and an LCDP[41] dataset containing over/under exposure images.

LOL-v2. LOL-v2 is divided into two subsets, LOL-v2-real and LOL-v2-Synthetic. The training and testing parts of LOL-v2-Real and LOL-v2-Synthetic are split proportionally into 689:100 and 900:100, respectively.

VILNC. VILNC is a new LLIE dataset [35], which comprises 115 indoor scenes and 20 outdoor scenes. Each indoor scene possesses three different brightness levels to simulate varying degrees of low-light images, with a normal brightness image used as a reference, while each outdoor scene only contains a pair of low/normal brightness images. We randomly extract 20% of the images from the

indoor scene as the testing set, and the rest as the training set. To compare the performance of various methods on VILNC dataset fairly, we retrain all methods in VILNC-Indoor by using their open-source code with default training parameters. Except for the method [45], QuadPrior, which is trained with large-scale datasets, we directly use its pre-training weight for inference.

SID. The official SID dataset [5] contains 5094 raw short-exposure images, each with a corresponding long-exposure reference image. We adopt its customized version subset (Sony-Total-Dark) [53], which transfers the raw format images to sRGB images without gamma correction.

LCDP. The LCDP [41] contains images with both over-exposed and under-exposed regions, comprising 1,733 images, which are split into 1,415 for training, 100 for validation, and 218 for testing.

Implementation Details. Our model TPCNet is implemented by PyTorch and is trained with the Adam optimizer ($\beta_1=0.9$ and $\beta_2=0.999$) for 1500 epochs by using a single NVIDIA 3090 or 4090 GPU. The initial learning rate is set to 2.5×10^{-4} and then steadily decreased to 1×10^{-7} by the

Table 2. Quantitative results for the LCDP [41], Sony-Total-Dark [5], MEF [29], NPE [42], LIME [11], DICM [20], and VV [39] datasets. The top-ranking score is in **bold**, and the second-ranking score is underlined; (·) represents the rank order.

| Methods | Sony-Total-Dark | | LCDP | | Methods | NIQE↓ | Unpaired MUSIQ↑ | PI↓ | FLOPs(G) | Overall rank |
|---------------------|-----------------|--------------|---------------|--------------|---------------------|-----------------|------------------|-----------------|-----------|--------------|
| | PSNR↑ | SSIM↑ | PSNR↑ | SSIM↑ | | | | | | |
| RUAS [25] | 10.456 | 0.086 | 13.981 | 0.633 | RUAS [25] | 5.248(6) | 51.275(5) | 3.955(6) | 0.83(2) | 5 |
| PairLIE [8] | 15.340 | 0.532 | 14.748 | 0.686 | ZERO-IG [35] | 3.987(4) | 47.618(6) | 3.542(5) | 11.37(4) | 5 |
| RetinexNet [50] | 18.230 | 0.596 | 19.626 | 0.689 | LANet [54] | 3.502(1) | 56.218(3) | 2.804(1) | 43.23(5) | <u>2</u> |
| ZeroDCE++ [22] | 12.683 | 0.082 | 12.223 | 0.668 | ZeroDCE++ [22] | 3.959(3) | 52.172(4) | 3.231(3) | 0.61(1) | 3 |
| HVI-CIDNet [53] | <u>22.904</u> | 0.676 | <u>22.840</u> | 0.846 | QuadPrior [45] | 4.666(5) | 62.241(1) | 3.455(4) | 1103.2(6) | 4 |
| TPCNet(Ours) | 23.577 | 0.691 | 23.398 | 0.874 | TPCNet(Ours) | <u>3.625(2)</u> | <u>58.070(2)</u> | <u>2.982(2)</u> | 8.76(3) | 1 |

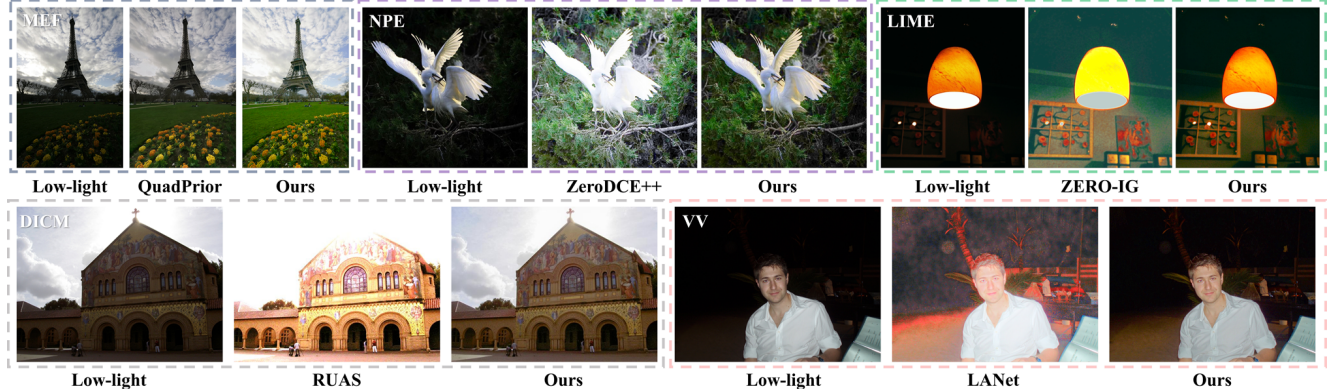


Figure 4. Visual comparison on the MEF [29], NPE [42], LIME [11], DICM [20], and VV [39] datasets.

cosine annealing scheme [28] during the training process. Patches of size 320×320 are randomly cropped from the low-/normal-light image pairs and the batch size is 8. The training data is augmented with flipping and random rotation. Inspired by reference [53], we utilize the loss function (L1 loss, perceptual loss [14], edge loss [34], and SSIM loss [48]) to supervise the enhanced result simultaneously in RGB space and specific color space.

Evaluation Metrics. For datasets with reference images, we exploit the peak signal-to-noise ratio (PSNR) and structural similarity (SSIM) [49] as the pixel-level evaluation and learned perceptual image patch similarity (LPIPS) [58] with AlexNet [18] as the perceptual quality evaluation. For the no-reference datasets, we evaluate the generalization of models trained on LOL-v2-Synthetic using various evaluation methods, such as natural image quality evaluator (NIQE) [32], multi-scale image quality transformer (MUSIQ) [17], and perceptual index (PI) [2]. We exploit PyTorch Toolbox [4] for calculating no-reference metrics.

4.2. Main Results

Quantitative Results. The quantitative results between our TPCNet and a wide range of SOTA enhancement algorithms are shown in Tables 1 and 2. Our TPCNet outperforms SOTA methods on LOL-v2 and VILNC-Indoor datasets in terms of almost all PSNR, SSIM, and LPIPS metrics, and possesses advantages in various metrics, such as NIQE, MUSIQ, and PI on no-reference datasets (MEF [29], NPE [42], LIME [11], DICM [20], and VV [39]), while requiring less computation.

For the reference datasets shown in Table 1, we com-

pared our results with the SOTA lightweight method HVI-CIDNet. Our TPCNet achieves 0.867 dB, 0.327 dB, and 0.978 dB improvements for approximately the same computational cost. Compared to RetinexFormer, a SOTA Retinex-based method, TPCNet realizes higher quality image enhancement and further expands its parameters 1.6 times (2.62/1.61), but only costs 56% (8.76/15.57) FLOPs, demonstrating that our CG-MSA is efficiently designed. Especially, in the real-world dataset VILNC-Indoor, TPCNet achieves over 15 dB improvement compared to the previous Retinex-based methods.

To verify TPCNet generalization on the no-reference datasets shown in Table 2, we compare our model with a recent SOTA unsupervised method. Compared to QuadPrior, which is trained on the large-scale datasets, TPCNet exhibits an obvious improvement in the NIQE and PI metric but only requires 0.8% (8.76/1103.2) of its FLOPs. Compared with other approaches, TPCNet shows the advantages in NIQE, MUSIQ, and PI metrics without a large computational consumption, achieving a balance between performance and efficiency. These results demonstrate that the TPC constructed on an implicit feature space can improve the generalization and robustness of our model.

Qualitative Results. The visual results for comparing TPCNet to other SOTA algorithms are shown in Figs. 3 and 4. From the Fig. 3 visualization, we can observe that TPCNet achieves stable brightness enhancement and maintains color consistency while other algorithms exhibit a certain flaw, especially in real-world datasets (VILNC-Indoor). For example, the earliest Retinex-based DL, RetinexNet, produces serious color deviation during enhancement when facing extreme darkness, while RetinexFormer recovers the

Table 3. Ablation on the LOLv2-real dataset. PSNR, SSIM, LPIPS, Params, and FLOPS (size = 256×256) are reported. The best results are marked in **bold** and the second best are underlined.

| Baseline-1 | CAM | LFE | RFE | TPC | PSNR↑ | SSIM↑ | LPIPS↓ | Params (M) | FLOPs (G) |
|------------|-----|-----|-----|-----|---------------|--------------|--------------|------------|-----------|
| ✓ | | | | | 21.637 | 0.854 | 0.119 | 1.65 | 5.72 |
| ✓ | ✓ | | | | 23.729 | 0.871 | 0.111 | 2.61 | 8.32 |
| ✓ | ✓ | ✓ | | | 24.232 | 0.876 | 0.111 | 2.61 | 8.46 |
| ✓ | ✓ | | ✓ | | 24.263 | 0.874 | 0.109 | 2.62 | 8.55 |
| ✓ | ✓ | ✓ | ✓ | | 24.357 | 0.881 | 0.099 | 2.62 | 8.68 |
| ✓ | ✓ | ✓ | ✓ | ✓ | 24.641 | 0.881 | <u>0.100</u> | 2.62 | 8.76 |

(a) Decomposed ablation of each component.

correct color, but still with a little color deviation. Compared to a recent SOTA algorithm, HVI-CIDNet can recover accurate color due to its HVI color space advantage, but some details are blurred.

In addition, visual comparisons between TPCNet and other SOTA supervised and unsupervised algorithms on five datasets without ground truth are illustrated in Fig. 4. For each dataset, we select one image to compare our method with a SOTA algorithm. From the results, we can see the shortcomings of the previous SOTA methods during the enhancement process, for example, overexposure/underexposure, color deviation, and amplified noise. In contrast, our TPCNet can effectively enhance low-light regions without introducing obvious spots and serious color deviation. These quantitative and qualitative results demonstrate the superior performance of TPCNet over previous SOTA methods in the lightweight LLIE field and demonstrate that the TPC constructed in implicit space can improve the performance and generalization of our model.

4.3. Ablation Study

We perform all ablation experiments on LOL-v2-Real for good convergence and stable performance of TPCNet. To verify the key modules, physical constraint, and the CAM with different color spaces in TPCNet, we use quantitative comparisons. The results are reported in Table 3.

Decomposed ablation. We utilize a decomposed ablation to analyze the effect of each component on improving performance, as displayed in Table 3a. To obtain Baseline-1, which only comprises the DCGT framework, we remove the CAM from TPCNet and replace its LFE and RFE with $conv3 \times 3$. Meanwhile, Eq. (3) is replaced by a $conv3 \times 3$ mapping the output from the last CGAB to the enhanced result, and Eqs. (4) and (5) are removed in TPCNet, to avoid the impact of physical constraint. When we exploit the CAM with HVI [53] as the color space, the mapping $conv3 \times 3$ is utilized to produce enhanced brightness instead of the final enhanced result. Baseline-1 realizes an obvious improvement, gaining 2.102 dB after applying CAM. Subsequently, we employ the LFE and RFE, respectively, and Baseline-1 achieves 2.605 and 2.636 dB improvements, respectively. When jointly applying these two estimators, the Baseline-1 achieves an increase of 2.730 dB. Subsequently, the TPC is introduced to obtain our final TPCNet version, and Baseline-1 realizes a 3.004 dB improvement.

| Metrics | | PSNR↑ | SSIM↑ | LPIPS↓ | Params (M) | FLOPs (G) |
|----------------------------|---------------|---------------|--------------|--------------|------------|-----------|
| Physical Constraint | w/o Eq. (3-5) | 24.357 | 0.881 | 0.099 | 2.62 | 8.68 |
| | w/o Eq. (3) | 24.598 | 0.881 | 0.101 | 2.62 | 8.76 |
| | w/o Eq. (4-5) | 24.575 | 0.876 | 0.110 | 2.62 | 8.68 |
| Color Space | HVI | <u>24.641</u> | 0.881 | <u>0.100</u> | 2.62 | 8.76 |
| | LAB | 24.588 | 0.873 | 0.114 | 2.62 | 8.76 |
| | YCBCR | 24.978 | 0.882 | 0.102 | 2.62 | 8.76 |

(b) Ablation studies on physical constraints and color space.

These decomposed experiments prove the effectiveness of CAM, LFE, RFE, and physical constraint in our TPCNet.

Physical constraint. To analyze the effect of TPC, we administer an ablation experiment to study each physical constraint. The quantitative results are exhibited in Table 3b. We first remove TPC from TPCNet, and initially obtain an PSNR of 24.357 dB. Then, we separately apply Eqs. (4) and (5) and Eq. (3) to form constraints on the inner network, and the model achieves a gain of 0.241 dB and 0.218 dB, respectively. Finally, we construct the complete TPC for further improvement. These results validate that exploiting physical constraints within the inner network can optimize performance without requiring additional parameters, simultaneously providing an interpretable method for network design.

Color spaces. We conduct ablation experiments to study the robustness of CAM with different color spaces and further explore its impact on model performance. Based on our image formation model, we chose a color conversion that can transform RGB images into a color space where brightness and color information can be separated, such as HVI [53], YCbCr [15], and LAB [38]. The corresponding quantitative results are presented in Table. 1b. Our results demonstrate the great robustness of CAM in various color spaces, and can achieve superior performance (the PSNR is 24.641 / 24.588 / 24.978 with Color space HVI / LAB / Ycbcr), better than the SOTA methods [3, 51, 53] in recent years.

5. Conclusion

In this work, we have reformulated the influence of physical constraints in the imaging process based on the Kubelka-Munk theory, and have constructed a the physical constraint among illumination, reflection, and detection. Our TPC theory addresses the limitations of previous Retinex-based algorithms, which view the reflected objects as ideal Lambertian and ignore the specular reflection coefficient in the modeling process. Extensive quantitative and qualitative experiments verify the effectiveness of our model in improving the robustness and LLIE ability by constructing physical constraints in feature space, and demonstrate that TPCNet outperforms SOTA LLIE methods on 10 datasets, thus expanding the interpretable network-design direction for low-light enhancement.

References

- [1] Partha Pratim Banik, Rappy Saha, and Ki-Doo Kim. Contrast enhancement of low-light image using histogram equalization and illumination adjustment. In *2018 International Conference on Electronics, Information, and Communication (ICEIC)*, pages 1–4, 2018. 1
- [2] Yochai Blau and Tomer Michaeli. The perception-distortion tradeoff. In *Proceedings of the IEEE conference on computer vision and pattern recognition*, pages 6228–6237, 2018. 7
- [3] Yuanhao Cai, Hao Bian, Jing Lin, Haoqian Wang, Radu Timofte, and Yulun Zhang. Retinexformer: One-stage retinex-based transformer for low-light image enhancement. In *Proceedings of the IEEE/CVF International Conference on Computer Vision (ICCV)*, pages 12504–12513, 2023. 1, 2, 4, 5, 6, 8
- [4] Chaofeng Chen and Jiadi Mo. IQA-PyTorch: Pytorch toolbox for image quality assessment. [Online]. Available: <https://github.com/chaofengc/IQA-PyTorch>, 2022. 7
- [5] Chen Chen, Qifeng Chen, Jia Xu, and Vladlen Koltun. Learning to see in the dark. In *2018 IEEE/CVF Conference on Computer Vision and Pattern Recognition*, pages 3291–3300, 2018. 6, 7
- [6] Alexey Dosovitskiy, Lucas Beyer, Alexander Kolesnikov, Dirk Weissenborn, Xiaohua Zhai, Thomas Unterthiner, Mostafa Dehghani, Matthias Minderer, Georg Heigold, Sylvain Gelly, Jakob Uszkoreit, and Neil Houlsby. An image is worth 16x16 words: Transformers for image recognition at scale, 2020. 5
- [7] Huiyuan Fu, Wenkai Zheng, Xiangyu Meng, Xin Wang, Chuanming Wang, and Huadong Ma. You do not need additional priors or regularizers in retinex-based low-light image enhancement. In *2023 IEEE/CVF Conference on Computer Vision and Pattern Recognition (CVPR)*, pages 18125–18134, 2023. 2, 4
- [8] Zhenqi Fu, Yan Yang, Xiaotong Tu, Yue Huang, Xinghao Ding, and Kai-Kuang Ma. Learning a simple low-light image enhancer from paired low-light instances. In *2023 IEEE/CVF Conference on Computer Vision and Pattern Recognition (CVPR)*, pages 22252–22261, 2023. 6, 7
- [9] Jan-Mark Geusebroek. Color and geometrical structure in images. *Appl. Microsc.*, 3, 2000. 2, 3
- [10] J.-M. Geusebroek, R. van den Boomgaard, A.W.M. Smeulders, and H. Geerts. Color invariance. *IEEE Transactions on Pattern Analysis and Machine Intelligence*, 23(12):1338–1350, 2001. 2, 3
- [11] Xiaojie Guo, Yu Li, and Haibin Ling. Lime: Low-light image enhancement via illumination map estimation. *IEEE Transactions on Image Processing*, 26(2):982–993, 2017. 1, 2, 4, 6, 7
- [12] Yifan Jiang, Xinyu Gong, Ding Liu, Yu Cheng, Chen Fang, Xiaohui Shen, Jianchao Yang, Pan Zhou, and Zhangyang Wang. Enlightengan: Deep light enhancement without paired supervision. *IEEE Transactions on Image Processing*, 30:2340–2349, 2021. 6
- [13] D.J. Jobson, Z. Rahman, and G.A. Woodell. Properties and performance of a center/surround retinex. *IEEE Transactions on Image Processing*, 6(3):451–462, 1997. 1, 2
- [14] Justin Johnson, Alexandre Alahi, and Li Fei-Fei. Perceptual losses for real-time style transfer and super-resolution. In *European conference on computer vision*, pages 694–711. Springer, 2016. 7
- [15] Amanpreet Kaur and BV Kranthi. Comparison between ycbcr color space and cielab color space for skin color segmentation. *International Journal of Applied Information Systems*, 3(4):30–33, 2012. 4, 8
- [16] Manpreet Kaur, Jasdeep Kaur, and Jappreet Kaur. Survey of contrast enhancement techniques based on histogram equalization. *International Journal of Advanced Computer Science and Applications*, 2(7), 2011. 1
- [17] Junjie Ke, Qifei Wang, Yilin Wang, Peyman Milanfar, and Feng Yang. Musiq: Multi-scale image quality transformer. In *2021 IEEE/CVF International Conference on Computer Vision (ICCV)*, pages 5128–5137, 2021. 7
- [18] Alex Krizhevsky, Ilya Sutskever, and Geoffrey E. Hinton. Imagenet classification with deep convolutional neural networks. *Commun. ACM*, 60(6):84–90, 2017. 7
- [19] Edwin H. Land. The retinex theory of color vision. *Scientific American*, 237(6):108–129, 1977. 2, 3, 4
- [20] Chulwoo Lee, Chul Lee, and Chang-Su Kim. Contrast enhancement based on layered difference representation of 2d histograms. *IEEE Transactions on Image Processing*, 22(12):5372–5384, 2013. 6, 7
- [21] Attila Lengyel, Sourav Garg, Michael Milford, and Jan C. van Gemert. Zero-shot day-night domain adaptation with a physics prior. In *Proceedings of the IEEE/CVF International Conference on Computer Vision (ICCV)*, pages 4399–4409, 2021. 2, 4
- [22] Chongyi Li, Chunle Guo, and Chen Change Loy. Learning to enhance low-light image via zero-reference deep curve estimation. *IEEE Transactions on Pattern Analysis and Machine Intelligence*, 44(8):4225–4238, 2022. 6, 7
- [23] Jinlong Li, Baolu Li, Zhengzhong Tu, Xinyu Liu, Qing Guo, Felix Juefei-Xu, Runsheng Xu, and Hongkai Yu. Light the night: A multi-condition diffusion framework for unpaired low-light enhancement in autonomous driving. In *Proceedings of the IEEE/CVF Conference on Computer Vision and Pattern Recognition*, pages 15205–15215, 2024. 1
- [24] Mading Li, Jiaying Liu, Wenhan Yang, Xiaoyan Sun, and Zongming Guo. Structure-revealing low-light image enhancement via robust retinex model. *IEEE Transactions on Image Processing*, 27(6):2828–2841, 2018. 2
- [25] Risheng Liu, Long Ma, Jiaao Zhang, Xin Fan, and Zhongxuan Luo. Retinex-inspired unrolling with cooperative prior architecture search for low-light image enhancement. In *2021 IEEE/CVF Conference on Computer Vision and Pattern Recognition (CVPR)*, pages 10556–10565, 2021. 6, 7
- [26] Yunlong Liu, Tao Huang, Weisheng Dong, Fangfang Wu, Xin Li, and Guangming Shi. Low-light image enhancement with multi-stage residue quantization and brightness-aware attention. In *2023 IEEE/CVF International Conference on Computer Vision (ICCV)*, pages 12106–12115, 2023. 1, 6
- [27] Ze Liu, Yutong Lin, Yue Cao, Han Hu, Yixuan Wei, Zheng Zhang, Stephen Lin, and Baining Guo. Swin transformer:

- Hierarchical vision transformer using shifted windows. In *2021 IEEE/CVF International Conference on Computer Vision (ICCV)*, pages 9992–10002, 2021. 5
- [28] Ilya Loshchilov and Frank Hutter. Sgdr: Stochastic gradient descent with warm restarts. *arXiv preprint arXiv:1608.03983*, 2016. 7
- [29] Kede Ma, Kai Zeng, and Zhou Wang. Perceptual quality assessment for multi-exposure image fusion. *IEEE Transactions on Image Processing*, 24(11):3345–3356, 2015. 6, 7
- [30] Long Ma, Tengyu Ma, Risheng Liu, Xin Fan, and Zhongxuan Luo. Toward fast, flexible, and robust low-light image enhancement. In *2022 IEEE/CVF Conference on Computer Vision and Pattern Recognition (CVPR)*, pages 5627–5636, 2022. 1
- [31] Youssef Mansour and Reinhard Heckel. Zero-shot noise2noise: Efficient image denoising without any data. In *2023 IEEE/CVF Conference on Computer Vision and Pattern Recognition (CVPR)*, pages 14018–14027, 2023. 5
- [32] Anish Mittal, Rajiv Soundararajan, and Alan C. Bovik. Making a “completely blind” image quality analyzer. *IEEE Signal Processing Letters*, 20(3):209–212, 2013. 7
- [33] Z. Rahman, D.J. Jobson, and G.A. Woodell. Multi-scale retinex for color image enhancement. In *Proceedings of 3rd IEEE International Conference on Image Processing*, pages 1003–1006 vol.3, 1996. 2
- [34] George Seif and Dimitrios Androustos. Edge-based loss function for single image super-resolution. In *2018 IEEE International Conference on Acoustics, Speech and Signal Processing (ICASSP)*, pages 1468–1472, 2018. 7
- [35] Yiqi Shi, Duo Liu, Liguozhang, Ye Tian, Xuezhi Xia, and Xiaojing Fu. Zero-ig: Zero-shot illumination-guided joint denoising and adaptive enhancement for low-light images. In *2024 IEEE/CVF Conference on Computer Vision and Pattern Recognition (CVPR)*, pages 3015–3024, 2024. 1, 2, 6, 7
- [36] Gursharn Singh, Anand Mittal, et al. Various image enhancement techniques—a critical review. *International Journal of Innovation and Scientific Research*, 10(2):267–274, 2014. 1
- [37] Alvy Ray Smith. Color gamut transform pairs. *SIGGRAPH Comput. Graph.*, 12(3):12–19, 1978. 4
- [38] M. Tkalcic and J.F. Tasic. Colour spaces: perceptual, historical and applicational background. In *The IEEE Region 8 EUROCON 2003. Computer as a Tool.*, pages 304–308 vol.1, 2003. 8
- [39] Vassilios Vonikakis, Rigas Kouskouridas, and Antonios Gasteratos. On the evaluation of illumination compensation algorithms. *Multimedia Tools and Applications*, 77(8):9211–9231, 2018. 6, 7
- [40] Chien-Yao Wang, I-Hau Yeh, and Hong-Yuan Mark Liao. Yolov9: Learning what you want to learn using programmable gradient information. In *European conference on computer vision*, pages 1–21. Springer, 2024. 1
- [41] Haoyuan Wang, Ke Xu, and Rynson WH Lau. Local color distributions prior for image enhancement. In *European conference on computer vision*, pages 343–359. Springer, 2022. 6, 7
- [42] Shuhang Wang, Jin Zheng, Hai-Miao Hu, and Bo Li. Naturalness preserved enhancement algorithm for non-uniform illumination images. *IEEE Transactions on Image Processing*, 22(9):3538–3548, 2013. 6, 7
- [43] Tao Wang, Kaihao Zhang, Tianrun Shen, Wenhan Luo, Bjorn Stenger, and Tong Lu. Ultra-high-definition low-light image enhancement: A benchmark and transformer-based method. In *Proceedings of the AAAI conference on artificial intelligence*, pages 2654–2662, 2023. 6
- [44] Wenjing Wang, Wenhan Yang, and Jiaying Liu. Hla-face: Joint high-low adaptation for low light face detection. In *2021 IEEE/CVF Conference on Computer Vision and Pattern Recognition (CVPR)*, pages 16190–16199, 2021. 1
- [45] Wenjing Wang, Huan Yang, Jianlong Fu, and Jiaying Liu. Zero-reference low-light enhancement via physical quadruple priors. In *2024 IEEE/CVF Conference on Computer Vision and Pattern Recognition (CVPR)*, pages 26057–26066, 2024. 1, 2, 3, 6, 7
- [46] Xinzhe Wang, Kang Ma, Qiankun Liu, Yunhao Zou, and Ying Fu. Multi-object tracking in the dark. In *2024 IEEE/CVF Conference on Computer Vision and Pattern Recognition (CVPR)*, pages 382–392, 2024. 1
- [47] Yinglong Wang, Zhen Liu, Jianzhuang Liu, Songcen Xu, and Shuaicheng Liu. Low-light image enhancement with illumination-aware gamma correction and complete image modelling network. In *2023 IEEE/CVF International Conference on Computer Vision (ICCV)*, pages 13082–13091, 2023. 1
- [48] Zhou Wang, A.C. Bovik, H.R. Sheikh, and E.P. Simoncelli. Image quality assessment: from error visibility to structural similarity. *IEEE Transactions on Image Processing*, 13(4): 600–612, 2004. 7
- [49] Zhou Wang, A.C. Bovik, H.R. Sheikh, and E.P. Simoncelli. Image quality assessment: from error visibility to structural similarity. *IEEE Transactions on Image Processing*, 13(4): 600–612, 2004. 7
- [50] Chen Wei, Wenjing Wang, Wenhan Yang, and Jiaying Liu. Deep retinex decomposition for low-light enhancement. In *British Machine Vision Conference*. British Machine Vision Association, 2018. 2, 3, 4, 6, 7
- [51] Xiaogang Xu, Ruixing Wang, Chi-Wing Fu, and Jiaya Jia. Snr-aware low-light image enhancement. In *2022 IEEE/CVF Conference on Computer Vision and Pattern Recognition (CVPR)*, pages 17693–17703, 2022. 1, 5, 6, 8
- [52] Xiaogang Xu, Ruixing Wang, and Jiangbo Lu. Low-light image enhancement via structure modeling and guidance. In *2023 IEEE/CVF Conference on Computer Vision and Pattern Recognition (CVPR)*, pages 9893–9903, 2023. 1, 6
- [53] Qingsen Yan, Yixu Feng, Cheng Zhang, Guansong Pang, Kangbiao Shi, Peng Wu, Wei Dong, Jinqiu Sun, and Yanming Zhang. Hvi: A new color space for low-light image enhancement. In *2025 IEEE/CVF Conference on Computer Vision and Pattern Recognition (CVPR)*, pages 5678–5687, 2025. 1, 3, 4, 5, 6, 7, 8
- [54] Kai-Fu Yang, Cheng Cheng, Shi-Xuan Zhao, Hong-Mei Yan, Xian-Shi Zhang, and Yong-Jie Li. Learning to adapt to light. *International Journal of Computer Vision*, 131(4): 1022–1041, 2023. 6, 7

- [55] Wenhan Yang, Wenjing Wang, Haofeng Huang, Shiqi Wang, and Jiaying Liu. Sparse gradient regularized deep retinex network for robust low-light image enhancement. *IEEE Transactions on Image Processing*, 30:2072–2086, 2021. [1](#), [2](#), [6](#)
- [56] Xunpeng Yi, Han Xu, Hao Zhang, Linfeng Tang, and Jiayi Ma. Diff-retinex: Rethinking low-light image enhancement with a generative diffusion model. In *Proceedings of the IEEE/CVF International Conference on Computer Vision*, pages 12302–12311, 2023. [2](#), [4](#)
- [57] Syed Waqas Zamir, Aditya Arora, Salman Khan, Munawar Hayat, Fahad Shahbaz Khan, and Ming-Hsuan Yang. Restormer: Efficient transformer for high-resolution image restoration. In *Proceedings of the IEEE/CVF conference on computer vision and pattern recognition*, pages 5728–5739, 2022. [1](#)
- [58] Richard Zhang, Phillip Isola, Alexei A Efros, Eli Shechtman, and Oliver Wang. The unreasonable effectiveness of deep features as a perceptual metric. In *Proceedings of the IEEE conference on computer vision and pattern recognition*, pages 586–595, 2018. [7](#)
- [59] Yonghua Zhang, Jiawan Zhang, and Xiaojie Guo. Kindling the darkness: A practical low-light image enhancer. In *Proceedings of the 27th ACM international conference on multimedia*, pages 1632–1640, 2019. [6](#)
- [60] Zunjin Zhao, Bangshu Xiong, Lei Wang, Qiaofeng Ou, Lei Yu, and Fa Kuang. Retinexdip: A unified deep framework for low-light image enhancement. *IEEE Transactions on Circuits and Systems for Video Technology*, 32(3):1076–1088, 2022. [2](#), [4](#)